Engineering Science and Technology, an International Journal 41 (2023) 101387

HOSTED BY

Contents lists available at ScienceDirect

Engineering Science and Technology, an International Journal

journal homepage: www.elsevier.com/locate/jestch

Wurtzite nanowires strain control by DC electrical stimulation

Giuseppe Prestopino [a,1], Pier Gianni Medaglia [a], David Scarpellini [b], Sergio Bietti [b], Pietro Oliva [c], Salvatore Monteleone [c], Andrea Orsini [c,*,1], Daniele Barettin [c], Federica Caselli [d], Paolo Bisegna [d]

[a] Industrial Engineering Department, University of Rome "Tor Vergata", Via del Politecnico,1, Rome 00133, Italy
[b] Materials Science Department, University of Milan "Bicocca", Piazza dell'Ateneo Nuovo, 1, Milan 20126, Italy
[c] ATHENA European University, University "Niccolò Cusano", Via Don Carlo Gnocchi, 3, Rome 00166, Italy
[d] Civil Engineering and Computer Science Department, University of Rome "Tor Vergata", Via del Politecnico,1, Rome 00133, Italy

ARTICLE INFO

Article history:
Received 15 December 2022
Revised 14 February 2023
Accepted 11 March 2023
Available online 21 March 2023

Keywords:
Nanowires
Young modulus
Elasticity
NEMS
GaAs

ABSTRACT

Nanomechanics is a highly developed area of research, given the significant reported changes in material properties at the nanometer scale, requiring the development of new theories to explain the underlying mechanisms. Such theories must be based on measurements that are as accurate as possible, but unfortunately, conventional experimental techniques do not apply to such small components. Here we present a unique new method to control electro-mechanical forces on quasi −1D nanostructures through static electric fields with multiple ways of control of GaAs nanowires' strain directly on the growth substrate.

1. Introduction

Peculiar mechanical properties are continuously emerging in nanoscaled materials [1–3], in particular, research on arrays of vertically aligned wurtzite nanowires widely increased because of their combined optoelectronic and piezoelectric properties [4–8], and the coupling with 2D materials like graphene and molybdenum disulphide [9–15]. Significant variance of mechanical properties with the scaling of size and dimensions has unfortunately been widely reported [16–18], posing new challenges to researchers trying to advance the design of micro- and nanoscale devices. In general, little attention was dedicated to the geometrical reconstruction of the tested nanowires. Instead, standard cylindrical shapes were often used to relate the applied force to the measured deflection. However, in such studies the force control is based on a diameter measured through the AFM scan distance without evaluating the polygon rotation angle along its central axe (see Fig. 1). In such a case, it is impossible to correctly evaluate the side length of the imaged nanowire which may vary within a percentage of more than 13% (see Fig. 1). Considering that the nanowires' size enters the expression of the area moment of inertia at the fourth power, an error of more than 50% may be obtained on the estimated elasticity value without considering any other error source. For this reason, in this research work, we focus on the geometrical reconstruction of the nanowire shape through the SEM control of the hexagonal edges position allowing length measurement and spatial orientation reconstruction of arrays of vertically aligned nanowires [19]. This approach provided nanowire geometrical information such as sides lengths, azimuth and elevation angle with unprecedented precision of less than 1 nm.

In order to perform force experiments with geometrical control over the nanowire shape, we opted for electrostatic deflections directly inside an electron microscope. In this technique, the bending is shown to be reversible and the force fully acting on the nanostructures tip protuberating toward the counterelectrode [20,21].

In this paper we further improve the electrostatic bending approach to prove nanostructures' elasticity directly on the growth substrate i.e., GaAs wurtzite nanowires grown on silicon substrates, to derive their internal strain. This study may be instrumental for piezo-optoelectronic devices involving quantum dots embedded into nanowire wurtzite lattice [22–28].

2. Methods

In this paper, we analyze quasi-1D nanostructures in the specific subcase of regularly shaped hexagonal GaAs nanowires grown

* Corresponding author.
E-mail address: andrea.orsini@unicusano.it (A. Orsini).
[1] Giuseppe Prestopino and Andrea Orsini contributed equally to this work.

https://doi.org/10.1016/j.jestch.2023.101387
2215-0986/

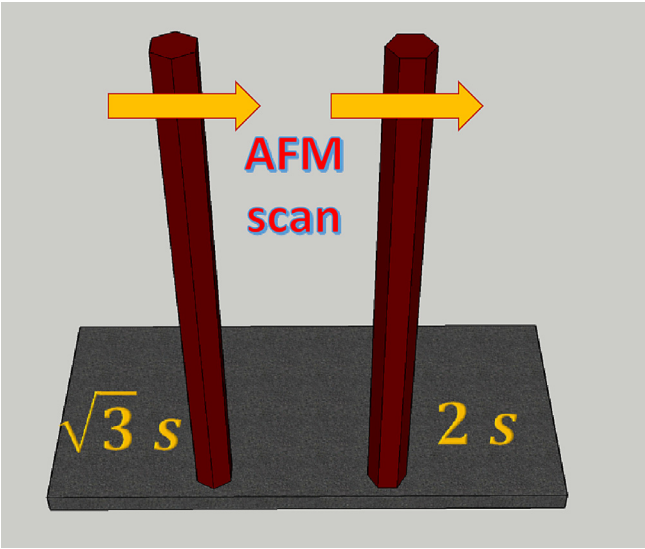

Fig. 1. Example of the two opposite position of nanowires hexagonal contour on behalf of the sample side: on the left a nanowire with edge termination on the front-view and on the right a nanowire with two parallel sides on the front-view.

by molecular beam epitaxy on (1 1 1) silicon substrates. Liquid Ga droplets assisted the growth of the GaAs nanowires [29].

Deflection experiments were performed into a Cambridge Stereoscan S260 SEM (Cambridge Instruments Ltd, Cambridge, UK), exploiting the possibility to operate an external sliding arm with at the end the tungsten ellipsoid used as a counterelectrode. Images were taken at 30 kV with resolution 768 × 576 pixel with color depth equal to 8 bit. 3D translation, tilt and rotation of the specimen stage were manually activated by control knobs. In order to maximize the resolution of the imaged nanowire deflection software image rotation (SR) was set through relative knob command. In addition to software rotation, a rotation angle (α_S) related to the working distance of the imaged nanowire was unavoidably present. Image rotation by a change in WD is a well-known effect in SEM microscopy, and it is due to changes in objective lens excitation to maintain focus [30].

Surface morphology was studied by a Zeiss LEO Supra 35 field emission gun scanning electron microscope (FEG SEM) by using the in-lens detector. The electron beam energy was set at 5 keV and the working distance at about 5 mm.

3. The model parameters

Based on the experimental setup described in section 2 we decided to apply the general theory of cantilever beams with concentrated load (P) at the free end to our deflection experiments. In fact, it was widely proven in literature [20,31] that semiconducting nanowires are able to concentrate the free charges available in the conduction band at the closest point of its crystal volume to the counterelectrode applying the electric field, which in our case is the nanowire tip. In such a case, neglecting elongation forces changing cross-section areas, the theory describing the bending of nanostructures with enhanced aspect-ratio should be represented by the following equation [32,33]:

$$M_{elas}(x) = \frac{E * I(x)}{\rho(x)} = P(L - x), \tag{1}$$

where $\rho(x)$ is the local curvature radius along the neutral line passing through the centers of mass of the cross section, E is the material Young modulus, $I(x)$ is the local second moment of area of the nanowire and L is the total length of the beam.

In case of $I(x) = const$ and small bending of the nanowire eq. (2) predicts for the maximum deflection at the tip (d_{tip}):

$$d_{tip} = \frac{P}{3EI} * L^3, if d_{tip} < \frac{1}{15}L \tag{2}$$

By the same model, we can calculate the angular change at the beam head that will be equal to:

$$\Delta\Omega_{tip} = \frac{P}{2 * E * I} * L^2 = \frac{3}{2} * \frac{d_{tip}}{L} \tag{3}$$

and the accumulated elastic energy and elastic force:

$$\Delta U_{nw} = \frac{P^2}{6 * E * I} * L^3 = \frac{3}{2} * \frac{EI}{L^3} * {d_{tip}}^2 \tag{4}$$

$$F_{elastic} = -\frac{\partial \Delta U_{nw}}{\partial d_{tip}} = -3 * \frac{EI}{L^3} * d_{tip} \tag{5}$$

We underline that in previous equations we are considering constant both the nanowires elastic properties along its length and the nanowire inertia moment. While the first assumption is very likely in the case of GaAs nanowires grown by MBE, the second one is only partially true. In fact, the nanowires present a slight pyramidal shape at the bottom, and this accounts for a decrease of $I(x)$ along its length, therefore in the next section we will define an averaged inertia moment to be used on behalf of I. On the other hand, looking to eq. (3) we notice that the force control depends on other parameters, each analyzed in the following different subsections:

1. Nanowire Length measurement (L) (section 3.2)
2. Tip Deflection Modeling (d_{tip}) (section 3.3)
3. Tip Electrical Load Modeling (P) (section 3.4)

3.1. Modeling of the Inertia moment

The most general approach to the modeling of the inertia moment of nanowires with different polygonal shapes [34–36], should consider the general integral equation for the evaluation of the second moment of area:

$$I(x_1) = \int^{area}\int p(x_2, x_3)^2 \delta x_2 \delta x_3 \tag{6}$$

where p($\boldsymbol{x}$) is the distance of the point with x_2, x_3 coordinates from the point x_1, over the neutral axis of rotation passing through the centroid of the cross-section. A nice method to evaluate automatically the sides of irregularly shaped hexagonal nanowires, typical result of wet-chemistry recipes, has been reported in [37]. However, in this paper we analyze quasi-1D nanostructures in the particular case of regularly shaped hexagonal GaAs nanowires grown by molecular beam epitaxy. Therefore, we directly applied the general theory of the mass moment of inertia, by considering a constant mass density along the nanowires and by evaluating mathematically the second moment of area of a filled regular hexagon with a side length of value (s). We obtain the following formula valid for any axes passing through the centroid:

$$I(x_1) = \sqrt{3} * s(x_1)^4 * \left(\frac{5}{16}\right) = 0.541 * s(x_1)^4 \tag{7}$$

In case of not constant $I(x)$, we have to substitute the value of I in previous equations with an equivalent quantity $\bar{I}$ evaluated through the double integral of the curvature:

$$\frac{L^3}{3\bar{I}} = \frac{1}{0.541} * \iint_0^L \frac{(L-x_1)}{s(x_1)^4}\delta x^2 \Rightarrow \bar{I} = 0.18 * \frac{1}{\int_0^L \frac{(1-x_1/L)}{\tilde{s}(x_1/L)^4}\delta(x_1/L)^2}$$

$$\bar{I} = 0.18/\iint_0^1 (1-f)/\tilde{s}(f)^4\delta^2(f); \quad (8)$$

where $f = x_1/L$ is the length fraction. Obviously, since the first antiderivative represents the angular deflection it is necessary to impose its additive unknown constant equal to 0 @ f = 0. As described in section 2.3, we performed the nanowire side measurements in a high resolution SEM by using in-lens focusing. In Fig. 2 we show the high-resolution SEM images of the nanowire whose deflection experiments will be shown in section 4 with a dedicated zoom in the central part of its body profile.

In Fig. 2a) it is possible to observe the entire profile of the GaAs nanowire, provided of a practically constant section along its central region, but with the base region appreciably larger. Furthermore, we observe also an increase of the side dimensions in the tip region. Even if this nanowire portion corresponds to the low moment arm of the applied force, it would still be an error neglecting the final section widening from the central body value of 131 nm (Fig. 2b). In the supplementary section 1 we report the mathematical modeling of a final linear broadening of the nanowire body, that demonstrates it cannot be neglected (possible error greater than 10%). Still more accuracy is required in modeling the section variation in the first part of the nanowire body because of the maximum moment arm present at the nanowire base.

In order to be as precise as possible, we performed the extraction of the nanowire section shape by calculating the SEM image scaling factor px/nm and extrapolating the physical distance of the side edges by the manual selection of a variable number of points (minimum of 10) on the imaged edge. Once reconstructed the nanowire edge shape, as the last step we have to correlate it to the side dimension s(x) of eq. (4). It is possible to see from the shadowing of the projected nanowire section we are practically observing the 2 s length of the nanowire hexagonal contour. The exact calculation of the real distance is reported in the supplementary section 2 and it confirms the estimated value of s(x) can be taken exactly on d(x)/2 (i.e. 65.5 nm in the central region). The shape of the nanowire body extracted thanks to the manual analysis can be corrected through the higher resolution reference value taken in Fig. 2b, as shown in the following Fig. 3. The $\bar{I}$ value mathematically reconstructed through eq. (8) is equal to 13.74 $\mu m^2 nm^2$ for the green line values and 11.84 $\mu m^2 nm^2$ for the red curve. As a comparison, the value of a straight beam with side equal to the center value (65.5 nm) would be equal to 9.96 $\mu m^2 nm^2$, almost 30% less.

3.2. Nanowire Length and 3D positioning

As preannounced in the methods section, the SEM where it is performed the deflection experiment suffers of backlashes in the motion mechanisms, therefore the determination of nanowire 3D positioning requires unidirectional SEM imaging at different tilting (see Fig. 4) just after the deflection experiments are terminated. Such analysis allows to precisely reconstruct the phi angle of the nanowire in the two used experimental configurations. Therefore, we started from the second experimental tilt angle t(1) ~ 20° and we performed other 5 images with 5° steps up to t(6) = 45°. The nanowire polar angles are unknown since the nanowire is selected after alignment with the counterelectrode already at the targeted angle of the deflection experiment.

It was confirmed in previous published paper on the same sample [19] that GaAs nanowires phi angle without any additive tilting of the SEM stage is 45.3° (φ_0), being vertically grown on a flat silicon substrate adhered to the 45° cut stub surface.

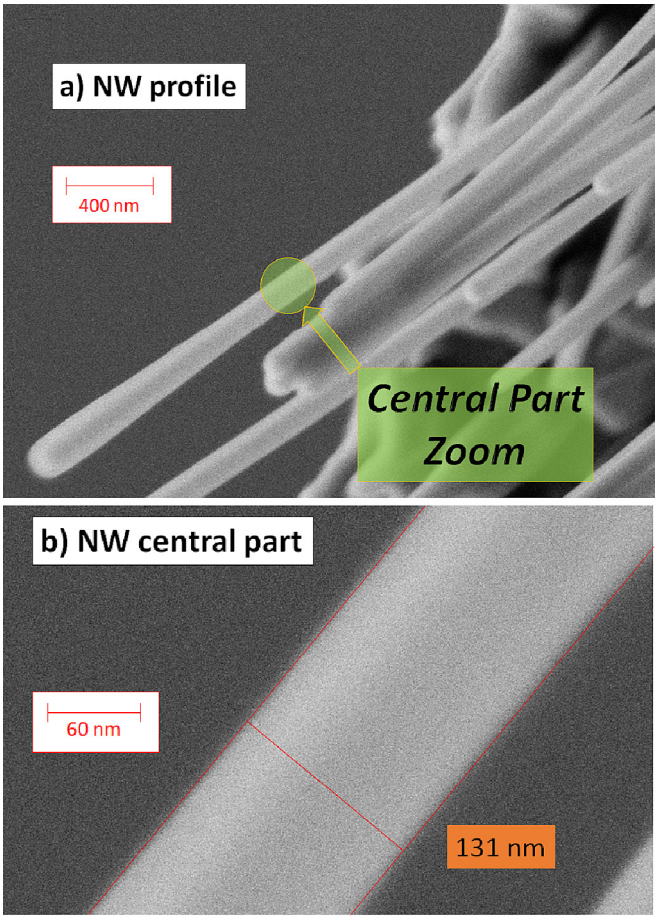

Fig. 2. High-resolution SEM images of the nanowire to be deflected (a) entire profile and (b) the central part.

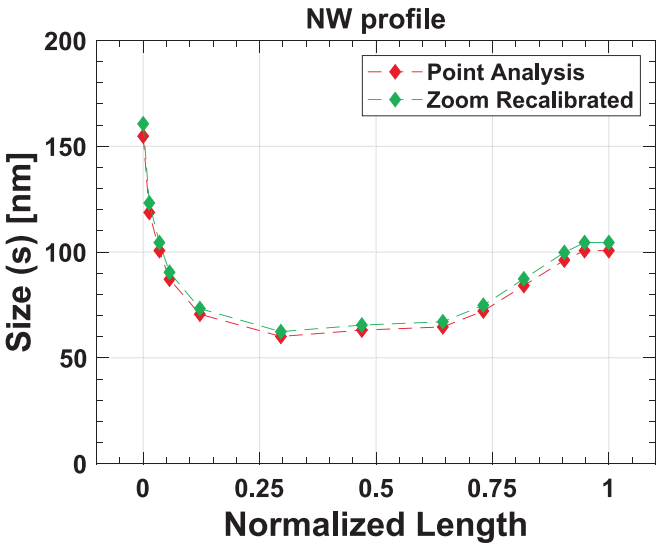

Fig. 3. Size profile of the GaAs nanowire according to its normalized length as derived from Fig. 2a) (red curve) and recalibrated proportionally through the value measured in the zoomed view of Fig. 2b). (For interpretation of the references to color in this figure legend, the reader is referred to the web version of this article.)

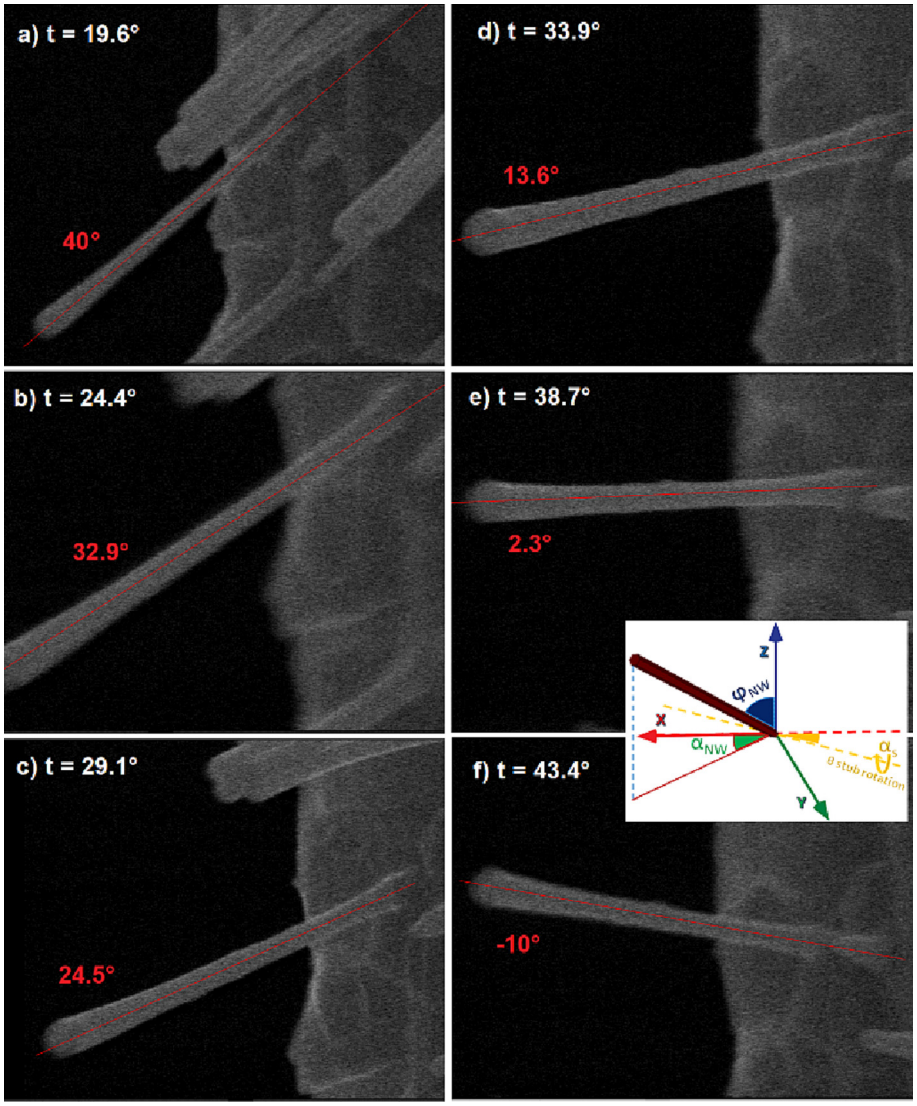

Fig. 4. Evaluation of the alpha angles of the nanowire in the SEM top-view at different tilt angles. In red color the measured values. In white color the applied tilting. (For interpretation of the references to color in this figure legend, the reader is referred to the web version of this article.)

With such a phi angle, with equal values of sine and cosine in first approximation, we can derive the following equation for the alpha angle of the SEM 2D projected nanowire when tilted at different theta angles:

$$NW_x \propto \left(\cos\theta_i cos{\alpha_S}^2 + sin{\alpha_S}^2\right)\sin\alpha_0$$

$$-0.5 sin2\alpha_S(1-cos\theta_i)cos\alpha_0 - cos\alpha_S \sin\theta_i;$$

$$NW_y \propto \left(\cos\theta_i sin{\alpha_S}^2 + cos{\gamma}^2\right)\cos\alpha_0$$

$$-0.5 sin2\alpha_S(1-cos\theta_i)sin\alpha_0 - sin\alpha_S \sin\theta_i;$$

$$\alpha_i = tan^{-1}\left(\frac{NW_y}{NW_x}\right); \quad (9)$$

where the α_S angle represent the misalignment between the imaged x-axis and the effective SEM tilt-axis, as described in the methods paragraph [19] and φ_0 is the unknown initial azimuthal angle. Through the building of a $\alpha(\theta)$ curve of values we can look for the best fitting according to the unknown parameters α_0 and α_S. By using just two measurements with wide theta difference, one taken in the last experimental condition (N2: θ = 19.6°) and one at about 45° upward tilting (precisely measured at θ = 43.4° by opening the SEM vacuum chamber), we extrapolated by Matlab fitting with the previous equations α_0 = 56.4°and α_S = 3°. Once we have determined the two aforementioned parameters we can calculate the nanowire phi-angle and the body length (L≈5270 nm) through the following equations:

$$NW_z \propto sin(\alpha_0+\alpha_S)\sin\theta_{exp} + \cos\theta_{exp}$$

$$\varphi_{exp} = tan^{-1}\left(\frac{\sqrt{{NW_y}^2 + {NW_x}^2}}{NW_z}\right). \quad (10)$$

In Table 1 we report the obtained values of the nanowire alpha and phi angles at the two different experimental conditions.

3.3. Modeling of the Tip deflection

We assume the load is concentrated on the final edges of the nanowire and that the electric field has to exit along a direction normal to the head conducting surfaces. In such a case, we can develop a model, as shown in Fig. 5, where the top hexagonal area

Table 1
GaAs nanowire 3D spherical angles in the deflection experiments.

Exp.	Tilt (°)	α (°)	φ (°)
n1	16	44.2	32.38
n2	19.6	40.0	29.83

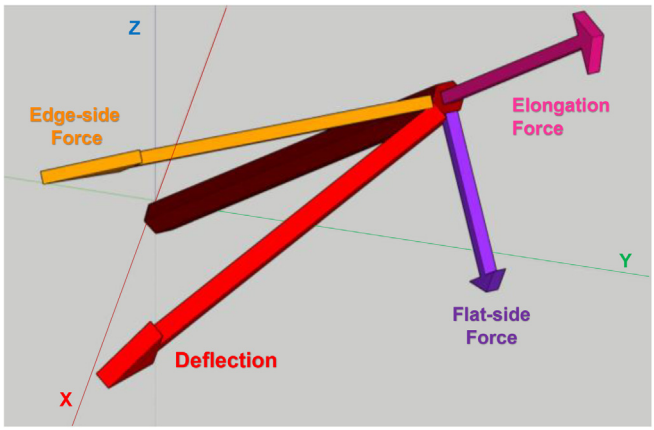

Fig. 5. Bending force vectors at the nanowire tip.

may contribute only to a negligible elongation due to the nanowire large aspect ratio difference, while the six side facets contribute to two different components of the load force that we define edge and flat forces. Substantially we are dividing the six sides of the GaAs nanowires regular hexagon into two different parts, one with two flat parallel sides and the second with four edged sides forming a 120° angle between each couple of them. Such nanowire position shown in Fig. 4 resembles the one used in the following experiments and it is important in order to maximize the force control.

Therefore, we can consider the deflection (red arrow) as composed by two components (Castigliano theorem): d_{flat} and d_{edge}, last one almost horizontal. The zeta coordinate variation of the nanowire head is calculated by nulling the projection along the elongation force vector (pink arrow). The obtained force unit vectors for last nanowire position corresponding to the second deflection experiment (N2) and for the precedent one corresponding to the first deflection experiment (N1) at a lower tilting angle calculated through the rotation matrix are reported in Table 2.

The previous assumptions obviously are specific to experiments related to nanowire with regular hexagonal geometries of the cross-section, because of their *iso*-directional area moment of inertia, as for the GaAs nanowires grown by MBE, and they of course need some adjustment for the general case of irregular hexagonally shaped nanowires.

3.4. Modeling of the Tip Coulombic Force

As described in section 2.2, we have to describe the load created by an electric potential difference between a semiconducting nanowire tip and a much larger metallic ellipsoid. Our approach bases on the consideration that the metallic ellipsoid appears practically flat to the smaller nanowire head area and it acts as a supposedly infinite conductive surface with fixed distance in the space along the x-axis. In this case, if we apply a constant voltage difference between the two parts we can use the electrostatic theory stating that the electrical force is obtained via the gradient of the energy:

Table 2
Force unit vectors in the deflection experiments.

Exp.	Edge	Flat	Elongation
n1 (X)	0.6449	0.5723	0.3325
n1 (Y)	−0.7630	0.4570	0.3234
n1 (Z)	0.0442	−0.4623	0.7313
Polar Angle χ	87.5°	147.7°	32.4°
Azimuthal Angle β	−49.79°	38.6°	44.2°
n2 (X)	0.6448	0.5738	0.3300
n2 (Y)	−0.7643	0.4850	0.2769
n2 (Z)	−0.0016	−0.4308	0.7513
Polar Angle χ	90.1°	150.2°	29.8°
Azimuthal Angle β	−49.85°	40.2°	40.0°

$$F_{nw}(V) = \frac{1}{2} * \frac{\partial C_{tip-ell}}{\partial u} * V^2 \tag{11}$$

In such a way the tip load depends only on the estimate of the applied potential and the tip-ellipsoid system, mainly dependent on the distance (a) between the tip and the counterelectrode, easily measurable by SEM imaging.

Our model assumes that the electrical force exerted on the nanowire tip would be almost proportional to the square value of the voltage apart of a coefficient k_V, close to unity, taking into account, according to the nanowire deformation with the applied voltage, both the small decrease of the tip-counterelectrode distance *a(V)* and the capacitance derivative change due to nanowire head rotation toward the counterelectrode:

$$F_{nw}(V_2) = k_V(\ 1) * (V_2/V_1)^2 F_{nw}(V_1) \tag{12}$$

In order to estimate the forces and the k_v coefficients of the two experiments, as stated in the introduction, we need to know precisely the tip distance from the counterelectrode. In Fig. 6 we report the panoramic picture of the nanowire array and the counterelectrode from which we evaluated the tip distance a(V1). The value of a(V2) was estimated directly by subtracting the Δx value of Table 3 (next section), from the value reported below, always considering the scan rotation angle of the SEM software:

$$\Delta x_{1,2} = (\Delta x(N1,2,V2) - \Delta x(N1,2,V1))$$

$$\Delta y_{1,2} = (\Delta y(N1,2,V2) - \Delta y(N1,2,V1))$$

$$a(V2,N1)(nm) = 7349 - \Delta x_1 * cos(SR1) - \Delta y_1 * \sin(SR1)$$

$$a(V2,N2)(nm) = 3262 - \Delta x_2 * cos(SR2) - \Delta y_2 * sin(SR2) \tag{13}$$

We can note in Fig. 6 that the ratio of the tip-counterelectrode distances is about 2.28, a value that perfectly compensates according to eq. (11) the 1.5 ratio between the voltages in the two different experiments (1.5^2 = 2.25). Following such ratio, we assume V_1 = 60 V and V_2 = 90 V at the largest distance (exp. N1) and V_1 = 40 V and V_2 = 60 V at the shortest distance (exp. N2). Therefore, if we suppose a linear proportionality between the capacitance derivative of the nanowire-ellipsoid system and their distance, we should obtain very close deflection values. The experimental results shown in Table 3 in the next section demonstrates that the linear inverse relationship between force and distance is almost verified.

In order to model the electrical force, as depicted in Fig. 5, we need to consider the two contributions of the flat sides and of the edged sides, with the latter expected to be larger because of the increasing charge density in small curvature regions of equipotential conducting surfaces [38]. The electrical field are obliged to exit normally from conducting surfaces therefore they have to follow the x-axis nearby the counterelectrode and the flat and edge

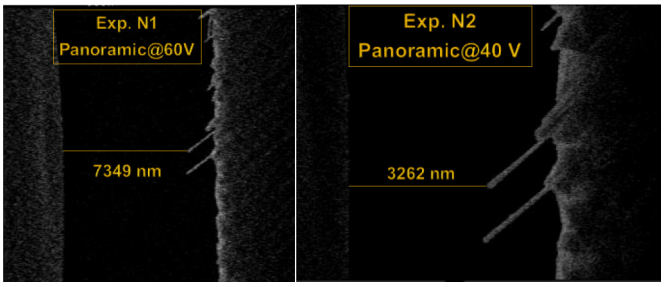

Fig. 6. Measurement of the nanowire tip → counter-electrode distance in the two different experiments (N1 left image; N2 right image) at the lower applied voltage. Images without any added software rotation (SR = 0).

unit vectors nearby the nanowire head (see Fig. 7), forming circumference arcs with the following angle and radius:

$$\Omega_{edge}(\mathrm{V}) = \cos^{-1}\left(\widehat{u_{edge}}(x)\right), R_{\overrightarrow{E}_{edge}}(V) = \frac{\mathrm{a(V)}}{sin\Omega_{edge}(V)} \tag{14}$$

$$\Omega_{flat}(\mathrm{V}) = \cos^{-1}\left(\widehat{u_{flat}}(x)\right), R_{\overrightarrow{E}_{flat}}(V) = \frac{\mathrm{a(V)}}{sin\Omega_{flat}(V)} \tag{15}$$

where Ω is the angle defined by the specific nanowire side and the counter-electrode normal and a is their distance (see Fig. 7).

According to the previous equations, the capacitance electrical field is inversely proportional to the counter-electrode distance and proportional to the following geometrical constraints:

$$C_{force}(V) = \varepsilon_0 * \frac{Aeq}{\Omega(V) * R_{\overrightarrow{E}}(V)} = \varepsilon_0 * Aeq * \frac{sin\Omega(V)}{a(V)\Omega(V)}. \tag{16}$$

On the other hand, up to now we just considered half of the capacitance area, while the hexagonal symmetry of the nanowire head accounts for other two contributing forces opposed to the previous ones with about same radius for the electric field lines but with supplementary arc angle and a δ increment of the edge distance from the counterelectrode:

$$C_{counterforce}(V) = \varepsilon_0 * Aeq * \frac{sin\Omega(V)}{(a(V)+\delta)(\pi - \Omega(V))} \tag{17}$$

$$\delta = 2 * s(head) * u_{edge}(x). \tag{18}$$

After having defined the main electric field lines in two normally directed contributions, we can evaluate each contribution separately assuming that the capacitance equivalent areas do not change with the small movements of the nanowire head. We can then express the capacitance derivative required in eq. (11) as a function of the edge deflection as:

$$\frac{\partial C_{tot}}{\partial u_{edge}} = \left(\frac{\partial C_{force}}{\partial u_{edge}} - \frac{\partial C_{counterforce}}{\partial u_{edge}}\right) =$$

$$\left(\frac{\partial C_{force}}{\partial \Omega} - \frac{\partial C_{counterforce}}{\partial \Omega}\right)\frac{\partial \Omega}{\partial u_{edge}} + \left(\frac{\partial C_{force}}{\partial a} - \frac{\partial C_{counterforce}}{\partial a}\right)\frac{\partial a}{\partial u_{edge}} \tag{19}$$

$$\frac{\partial C_{force}}{\partial \Omega} = C_{force} * (cot\Omega - 1/\Omega) \tag{20}$$

$$\frac{\partial C_{counterforce}}{\partial \Omega} = C_{counterforce} * \left(cot\Omega + \frac{1}{\pi - \Omega}\right) \tag{21}$$

$$\frac{\partial C_{counterforce}}{\partial \mathrm{a}} = -\frac{C_{counterforce}}{a(V)+\delta}; \frac{\partial C_{force}}{\partial \mathrm{a}} = -\frac{C_{force}}{a} \tag{22}$$

$$\frac{\partial a}{\partial u_{edge}} = -cos\Omega; \frac{\partial \Omega}{\partial u_{edge}} = \frac{1.5}{L}\frac{\widehat{u_{edge}(y)} * \widehat{u_{flat}(z)} - \widehat{u_{edge}(z)} * \widehat{u_{flat}(y)}}{sin\Omega} \tag{23}$$

where the last equation is derived through eq. (14) and the first order approximation of the rotation matrix with the applied tilt calculated through eq. (3). Since the edge force is practically horizontal it could be also almost correct in this and other similar experiments to assume last derivative equal to 1.5*sin(φ)/L. We note that just using the relative value of Ω angle, same equations can express the capacitance derivative as a function of the deflection in the flat side direction. Since the deflection along the flat side cannot be completely perceived from the SEM top-view we concentrate the force analysis on the edge deflection that instead is practically horizontal. In fact, the low resolution of the SEM images in the experimental condition does not allow a perfect alignment of the pixels on the x-axis (see Figs. 7-8) and this possible error due to our limited experimental availability reflects in majority over the flat-side direction control. However, the model can be applied independently on the two capacitance direction and then we can model the edge-sides total capacitance derivative with eq. (19). Unfortunately, in eq. (11) we have still a value that is unknown, i.e. the capacitance equivalent area including edge effects practically impossible to be geometrically modeled in an accurate way. On the other hand, in order to have control over the exerted coulombic force and bypass this problem, it is possible to apply a two voltages approach, with the first experiment only dedicated to extrapolate the C_{force} value. Then, by applying the previous equations we can calculate the coefficient k_v of eq. (12) and predict the nanowire experimental deflection at the omega angles of the second voltage.

4. Nanowire bending evaluation

A first experiment was performed with a tilt of about 20° along the SEM tilting axis. In Fig. 8 we report the experimental image of the undeflected nanowire (Fig. 8a) and its superimposition with the image taken with a relative applied voltage of 60 V and 90 V (Fig. 8b-c). Thanks to the MATLAB superimposition of the three images based on substrate edge profile alignment, we estimated the relative (Δx; Δy) tip deviation. In order to obtain a different deflection effect over the nanowire tip a second experiment was performed with a lower tilt angle of about 16° (Fig. 9). The lower nanowire-counterelectrode distance chosen approximately with a reduction factor of 1.5^2 makes the tip more sensitive to the applied voltage of 40 V and 60 V (Fig. 9b-c).

Table 3
GaAs nanowire deflection measurements.

Exp.	Voltage (V)	Δx (nm)	Δy (nm)	Δu_{edge} (nm)	k_v (theory)
N1(d_1)	V1 = 60	51.9	−42.6	61.4	
N1(d_2)	V2 = 90	125.4	−88.8	135.7	
(d_2/d_1)	Ratio normalized to the sq. voltage			0.9823	0.9689
N2(d_1)	V1 = 40	76.5	−55.1	86.1	
N2(d_2)	V2 = 60	152.7	−123.2	183.3	
(d_2/d_1)	Ratio normalized to the sq. voltage			0.9461	0.9081

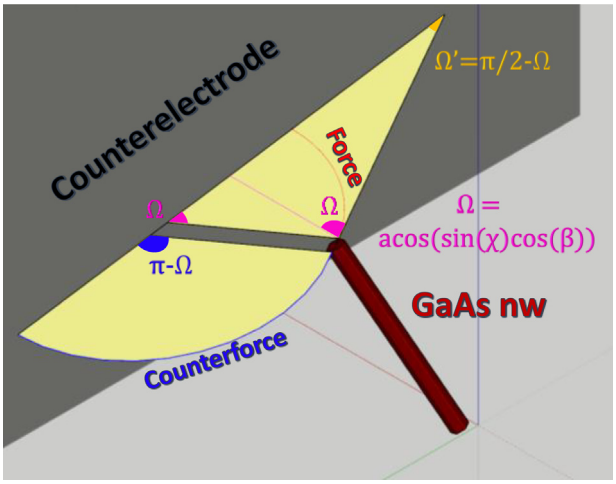

Fig. 7. Representation of the experimental electric field lines from the nanowire head toward the counter-electrode accounting for tip side area with exposed edge.

It is clearly visible in the experiments shown in Fig. 8 and Fig. 9 that in both tilting conditions the electrical force acts as expected with a larger edge contribution. In Table 3 we report the extrapolated tip deviation (Δx; Δy) (see supplementary section 3) and their projection over the nanowire edge axe. By considering the ratio of the extrapolated deflections in the same experiment (third row), the edge forces of both experiments change with the applied voltage with a coefficient lower than unity ($k_v < 1$). Recalling eq. (23) and the assumption that is possible to neglect capacitance equivalent area variations due to the change of the nanowire head spherical coordinates during its deflection we can state that:

$$k_{v,edge} = \frac{\partial C}{\partial u_{edge}}(V2) / \frac{\partial C}{\partial u_{edge}}(V1). \tag{24}$$

In order to evaluate the correct k_v value according to the 3D movement of the nanowire head, we used the additional correction of Table S1 (see supplementary section 3) to the Ω value to be used in eq. (24). We can observe that the experimental trend is well predicted by eq. (24), which calculated value is reported in the last column of Table 3.

The reported values also demonstrates that the supposed inverse proportionality between the applied coulombic force and the tip–counterelectrode distance is practically verified since the ratio calculated through Table 3 values is equal to 1.4 at V1 and 1.35 at V2, that is enough closer to 1 than to the programmed distance change (about 2.28, see Fig. 5). The difference between the two experiments is not related only to the distance between the nanowire tip and the counterelectrode but also to the nanowire head rotation toward the x-axis.

Once the tip deflection is known and predictable, it is possible to use tip-load equations to calculate the strain of each section of the nanowire body and apply the desired strain in the point of interest, i.e. a quantum dot heterostructure. Finally, by considering the Young modulus bulk value of GaAs (85.5 GPa) [39], we can derive the accumulated elastic energy (eq. 4–5) and thereby, the unknown capacitance equivalent area for the edge side. The obtained values taken at the maximum strain (V2) for both experiments are 11.6 μm^2 for exp. N1 and 8.3 μm^2 for exp. N2. The higher value for exp. N1 is plausible because of the higher alpha angle and major edge exposition toward the x-axis, on the other hand, the esteemed equivalent area coefficient of both experiments seems a bit too large. In fact, it is very plausible that the Young modulus of the nanowires grown by MBE studied in this paper is much closer to the 45 GPa reported for singly clamped inverted conical GaAs nanowires [40].

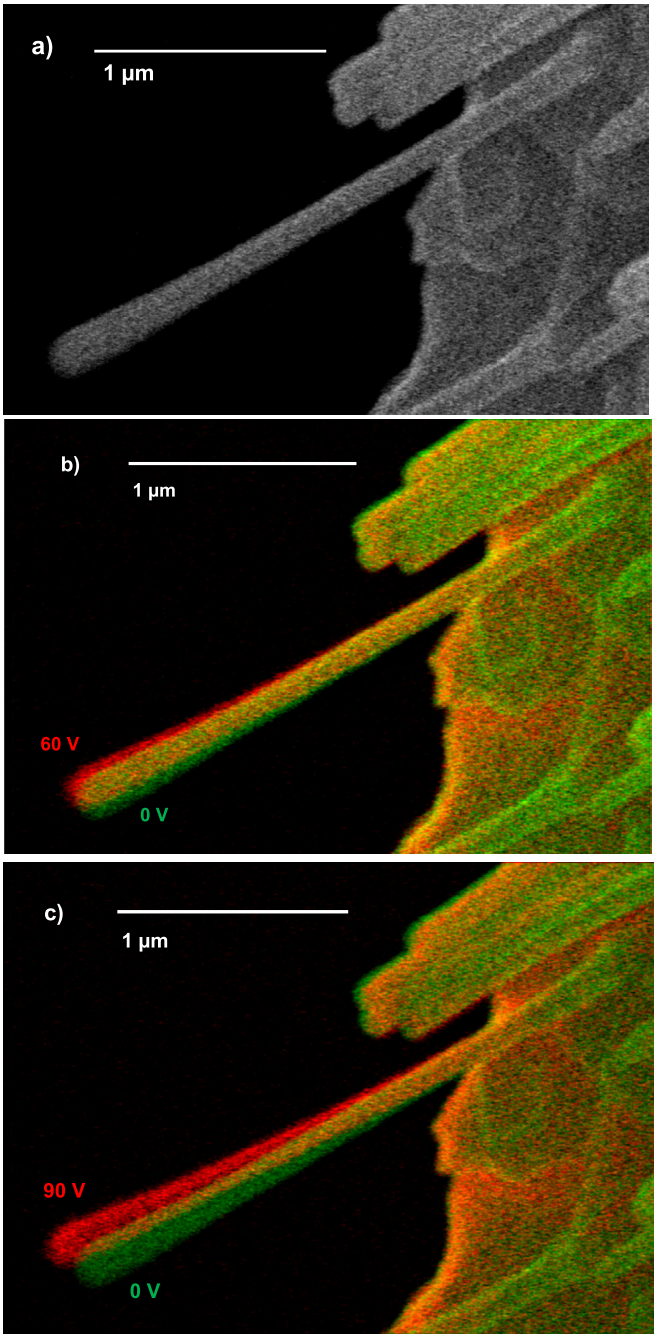

Fig. 8. Exp. N1 GaAs nanowire deflections at 20° tilting. a) 0 V applied, b) superimposition of figure a) (changed to green color) and the image taken with an applied voltage of 60 V (red color), c) superimposition of figure a) (green) and the image taken with an applied voltage of 90 V (red). (For interpretation of the references to color in this figure legend, the reader is referred to the web version of this article.)

5. Conclusions

In this paper, we deeply analyzed the problem of controlling mechanical deflections on hexagonally shaped semiconducting wurtzite nanowires evidencing the accuracy required in modeling all the geometrical parameters in the best possible way, especially the side length (s) that is involved into the beam equations to the

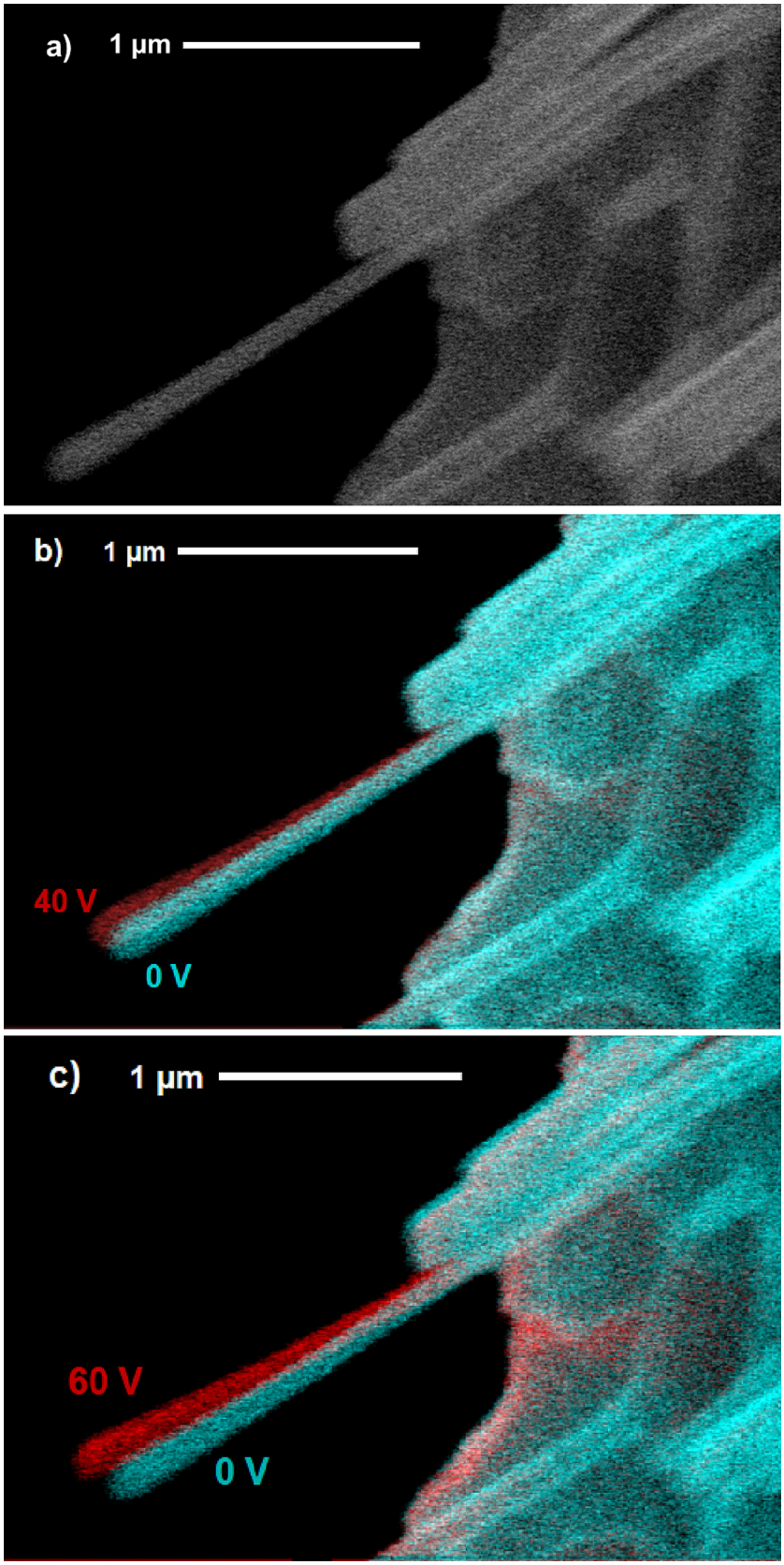

Fig. 9. Exp. N2 GaAs nanowire deflections at 16° tilting. a) 0 V applied, b) superimposition of figure a) (changed to aquamarine color) and the image taken with an applied voltage of 40 V (red color), c) superimposition of figure a) (aquamarine) and the image taken with an applied voltage of 60 V (red). (For interpretation of the references to color in this figure legend, the reader is referred to the web version of this article.)

fourth power. As reported in the literature, we also found that in electrostatic deflection of quasi-1D nanostructures the model to be used to control the deflection forces is that of cantilever beams with a concentrated load at the nanostructures free end. The force vector changes in its relative intensity and therefore in its direction according to the applied voltage. In particular, nanowire deflection toward the counterelectrode and the consequent more symmetric exposition of its facets surfaces accounts for a decreasing of the capacitance derivative. With the only basic assumption that the capacitance equivalent area remains constant despite the small geometrical variation of the electric fields we forecast force changes with good precision.

Such a method developed for hexagonally shaped wurtzite nanorods is likely to be extendable to other type of more complex nanowire shapes like zincblende [41] or pyramidal stars [42] by simply changing the area moment of inertia calculus and by looking for the main edges in the nanowires head termination. We also stress that the easy implementation of the designed experiments in modern high-resolution SEM would further enhance the capability of force determination as the development and refining of advanced force models. Furthermore, by extending the experimental setup capabilities with dynamic current measurements during electrostatic deflection voltage ramp, we infer the possibility by this technique to precisely measure the young modulus of quasi 1D nanostructures.

Declaration of Competing Interest

The authors declare that they have no known competing financial interests or personal relationships that could have appeared to influence the work reported in this paper.

Acknowledgments

The authors acknowledge Prof. Francesca Giannone for precious suggestions about the use of 3D rotation matrix. A.O. acknowledges financial support from ATHENA European University (EPLUS2020-AG, Project 101004096). P.B. acknowledges the financial support of MIUR, Italy, PRIN 2017 program, project 3DP_Future (grant 2017L7X3CS_004).

Appendix A. Supplementary data

Supplementary data to this article can be found online at https://doi.org/10.1016/j.jestch.2023.101387.

References

[1] A. Banerjee, D. Bernoulli, H. Zhang, M.-F. Yuen, J. Liu, J. Dong, F. Ding, J. Lu, M. Dao, W. Zhang, Y. Lu, S. Suresh, Ultralarge elastic deformation of nanoscale diamond, Science 80 (360) (2018) 300–302, https://doi.org/10.1126/science.aar4165.

[2] H. Zhang, J. Tersoff, S. Xu, H. Chen, Q. Zhang, K. Zhang, Y. Yang, C.S. Lee, K.N. Tu, J. Li, Y. Lu, Approaching the ideal elastic strain limit in silicon nanowires, Sci. Adv. 2 (2016) 2–10, https://doi.org/10.1126/sciadv.1501382.

[3] Y. Xing, L. Luo, Y. Li, D. Wang, D. Hu, T. Li, H. Zhang, Exploration of Hierarchical Metal-Organic Framework as Ultralight, High-Strength Mechanical Metamaterials, J. Am. Chem. Soc. 144 (2022) 4393–4402, https://doi.org/10.1021/jacs.1c11136.

[4] S. Chu, G. Wang, W. Zhou, Y. Lin, L. Chernyak, J. Zhao, J. Kong, L. Li, J. Ren, J. Liu, Electrically pumped waveguide lasing from ZnO nanowires, Nat. Nanotechnol. 6 (2011) 506–510, https://doi.org/10.1038/nnano.2011.97.

[5] W. Wu, X. Wen, Z.L. Wang, Taxel-addressable matrix of vertical-nanowire piezotronic transistors for active and adaptive tactile imaging, Science 340 (2013) 952–957, https://doi.org/10.1126/science.1234855.

[6] A. Orsini, P.G. Medaglia, D. Scarpellini, R. Pizzoferrato, C. Falconi, Towards high-performance, low-cost quartz sensors with high-density, well-separated, vertically aligned ZnO nanowires by low-temperature, seed-less, single-step, double-sided growth, Nanotechnology 24 (2013). http://www.scopus.com/inward/record.url?eid=2-s2.0-84895847908&partnerID=tZOtx3y1 355503.

[7] R.F. Service, Performance of Nanowire Solar Cells on the Rise, Science 339 (6117) (2013) 263.

[8] K.H. Li, X. Liu, Q. Wang, S. Zhao, Z. Mi, Ultralow-threshold electrically injected AlGaN nanowire ultraviolet lasers on Si operating at low temperature, Nat. Nanotechnol. 10 (2015) 140–144, https://doi.org/10.1038/nnano.2014.308.

[9] X. Huang, Z. Yin, S. Wu, X. Qi, Q. He, Q. Zhang, Q. Yan, F. Boey, H. Zhang, Graphene-Based Materials: Synthesis, Characterization, Properties, and Applications, Small 7 (2011) 1876–1902, https://doi.org/10.1002/smll.201002009.

[10] Y. Wu, X. Yan, X. Zhang, X. Ren, A monolayer graphene/GaAs nanowire array Schottky junction self-powered photodetector, Appl. Phys. Lett. 109 (18) (2016) 183101.

[11] A. Chakraborty, A. Agresti, R. Pizzoferrato, F. De Matteis, A. Orsini, P.G. Medaglia, Study of structural and optical properties of low temperature photo-activated ZnO-rGO composite thin film, Mater. Res. Bull. 91 (2017) 227–231, https://doi.org/10.1016/j.materresbull.2017.03.030.

[12] P.A. Alekseev, M.S. Dunaevskiy, A.O. Mikhailov, S.P. Lebedev, A.A. Lebedev, I.V. Ilkiv, A.I. Khrebtov, A.D. Bouravleuv, G.E. Cirlin, Electrical Properties of GaAs Nanowires Grown on Graphene/SiC Hybrid Substrates, Semiconductors 52 (2018) 1611–1615, https://doi.org/10.1134/S1063782618120047.

[13] Y. Luo, X. Yan, J. Zhang, B. Li, Y. Wu, Q. Lu, C. Jin, X. Zhang, X. Ren, A graphene/single GaAs nanowire Schottky junction photovoltaic device, Nanoscale 10 (2018) 9212–9217, https://doi.org/10.1039/C8NR00158H.

[14] A. Chakraborty, R. Pizzoferrato, A. Agresti, F. De Matteis, A. Orsini, P.G. Medaglia, Wet-Chemical Synthesis of ZnO Nanowires on Low-Temperature Photo-Activated ZnO-rGO Composite Thin Film with Enhanced Photoconduction, J. Electron. Mater. 47 (2018) 5863–5869, https://doi.org/10.1007/s11664-018-6473-5.

[15] A. Mukherjee, H. Yun, D.H. Shin, J. Nam, A.M. Munshi, D.L. Dheeraj, B.-O. Fimland, H. Weman, K.S. Kim, S.W. Lee, D.-C. Kim, Single GaAs Nanowire/Graphene Hybrid Devices Fabricated by a Position-Controlled Microtransfer and an Imprinting Technique for an Embedded Structure, ACS Appl. Mater. Interfaces 11 (2019) 13514–13522, https://doi.org/10.1021/acsami.8b20581.

[16] F. Xu, Q. Qin, A. Mishra, Y. Gu, Y. Zhu, Mechanical properties of ZnO nanowires under different loading modes, Nano Res. 3 (2010) 271–280, https://doi.org/10.1007/s12274-010-1030-4.

[17] F. Liu, D. Tang, H. Gan, X. Mo, J. Chen, S. Deng, N. Xu, Y. Bando, D. Golberg, O. Materials, D. Material, I. Nanostructured, M. Group, M. Nanoarchirectonics, M. Science, Y. Scientists, N. Group, Individual Boron Nanowire Has Ultra- High Speci fi c Young ' s Modulus and Fracture Strength As Revealed by in Situ, (2013) 10112–10120.

[18] W.M. Choi, K.-S. Shin, H.S. Lee, D. Choi, K. Kim, H.-J. Shin, S.-M. Yoon, J.-Y. Choi, S.-W. Kim, Selective growth of ZnO nanorods on SiO2/Si substrates using a graphene buffer layer, Nano Res. 4 (2011) 440–447, https://doi.org/10.1007/s12274-011-0100-6.

[19] G. Prestopino, A. Orsini, C. Falconi, S. Bietti, G. Verona-Rinati, F. Caselli, P. Bisegna, Length measurement and spatial orientation reconstruction of single nanowires, Nanotechnology 29 (37) (2018) 375704.

[20] P. Poncharal, Z.L. Wang, D. Ugarte, W.A. de Heer, Electrostatic Deflections and Electromechanical Resonances of Carbon Nanotubes, Science 283 (5407) (1999) 1513–1516.

[21] E.W. Wong, P.E. Sheehan, C.M. Lieber, Nanobeam Mechanics: Elasticity, Strength, and Toughness of Nanorods and Nanotubes, Science 277 (5334) (1997) 1971–1975.

[22] P. Kuyanov, S.A. McNamee, R.R. LaPierre, GaAs quantum dots in a GaP nanowire photodetector, Nanotechnology 29 (12) (2018) 124003.

[23] E.S. Semenova, I.V. Kulkova, S. Kadkhodazadeh, D. Barettin, O. Kopylov, A. Cagliani, K. Almdal, M. Willatzen, K. Yvind, Epitaxial growth of quantum dots on InP for device applications operating at the 1.55 μm wavelength range, Quantum Dots Nanostructures Synth. Charact. Model. XI. 8996 (2014), https://doi.org/10.1117/12.2039567 899606.

[24] D. Barettin, M.A. der Maur, A. di Carlo, A. Pecchia, A.F. Tsatsulnikov, A.V. Sakharov, W.V. Lundin, A.E. Nikolaev, S.O. Usov, N. Cherkashin, M.J. Hÿtch, S.Y. Karpov, Influence of electromechanical coupling on optical properties of InGaN quantum-dot based light-emitting diodes, Nanotechnology 28 (2017) 15701, https://doi.org/10.1088/0957-4484/28/1/015701.

[25] D. Barettin, M. Auf der Maur, A. di Carlo, A. Pecchia, A.F. Tsatsulnikov, W.V. Lundin, A.V. Sakharov, A.E. Nikolaev, M. Korytov, N. Cherkashin, M.J. Hÿtch, S.Y. Karpov, Carrier transport and emission efficiency in InGaN quantum-dot based light-emitting diodes, Nanotechnology 28 (27) (2017) 275201.

[26] D. Barettin, A.V. Platonov, A. Pecchia, V.N. Kats, G.E. Cirlin, I.P. Soshnikov, A.D. Bouravleuv, L. Besombes, H. Mariette, M.A. Der Maur, A. Di Carlo, Modelling of GaAs quantum dot embedded in a polymorph AlGaAs nano wire, 13th Int, Conf. Numer. Simul. Optoelectron. Devices, NUSOD 2013 (2013) 139–140, https://doi.org/10.1109/NUSOD.2013.6633163.

[27] G.E. Cirlin, R.R. Reznik, I.V. Shtrom, A.I. Khrebtov, I.P. Soshnikov, S.A. Kukushkin, L. Leandro, T. Kasama, N. Akopian, AlGaAs and AlGaAs/GaAs/AlGaAs nanowires grown by molecular beam epitaxy on silicon substrates, J. Phys. D Appl. Phys. 50 (48) (2017) 484003.

[28] D. Barettin, A. Pecchia, M. Auf der Maur, A. Di Carlo, B. Lassen, M. Willatzen, Electromechanical field effects in InAs/GaAs quantum dots based on continuum k→·p→ and atomistic tight-binding methods, Comput. Mater. Sci 197 (2021), https://doi.org/10.1016/j.commatsci.2021.110678 110678.

[29] D. Scarpellini, C. Somaschini, A. Fedorov, S. Bietti, C. Frigeri, V. Grillo, L. Esposito, M. Salvalaglio, A. Marzegalli, F. Montalenti, E. Bonera, P.G. Medaglia, S. Sanguinetti, InAs/GaAs Sharply Defined Axial Heterostructures in Self-

Assisted Nanowires, Nano Lett. 15 (2015) 3677–3683, https://doi.org/10.1021/nl504690r.
[30] Scanning Electron Microscopy and X-ray Microanalysis, 2003.
[31] D. Cohen-Tanugi, A. Akey, N. Yao, Ultralow superharmonic resonance for functional nanowires, Nano Lett. 10 (2010) 852–859, https://doi.org/10.1021/nl903302q.
[32] E.S. Carrillo, The cantilevered beam: An analytical solution for general deflections of linear-elastic materials, Eur. J. Phys. 27 (2006) 1437–1445, https://doi.org/10.1088/0143-0807/27/6/017.
[33] V. Vargas-Calderón, A.F. Guerrero-González, F. Fajardo, Measurement of Young's Modulus in Noodles and Bucatini, Phys. Educ. 01 (02) (2019) 1950010.
[34] H.-B. Wang, F. Ma, L. Zhou, Y. Qin, Y.-S. Sun, Y.-K. Xu, Y.-N. Chen, K.-W. Xu, D.-Y. Ma, Polar surface dominated octagonal Sn doped ZnO nanowires and their room-temperature photoluminance properties, Appl. Surf. Sci. 476 (2019) 265–270, https://doi.org/10.1016/j.apsusc.2018.12.282.
[35] E. Ochoa, D. Alducin, J.E. Sanchez, C. Fernando, U. Santiago, A. Ponce, Semiconductor behavior of pentagonal silver nanowires measured under mechanical deformation, J. Nanoparticle Res. 21 (2019) 134, https://doi.org/10.1007/s11051-019-4577-3.
[36] A. Orsini, C. Falconi, Real-time monitoring of the solution growth of ZnO nanorods arrays by quartz microbalances and in-situ temperature sensors, Sci. Rep. 4 (2014) 6285, https://doi.org/10.1038/srep06285.
[37] A. Mencattini, A. Orsini, C. Falconi, 3D Reconstruction of Quasi-1D Single-Crystal Nanostructures, Adv. Mater. 27 (40) (2015) 6271–6276.
[38] E. Durand, Electrostatique des conducteurs, Masson, 1966.
[39] https://www.memsnet.org/material/galliumarsenidegaasbulk/, (n.d.).
[40] P. Paulitschke, N. Seltner, A. Lebedev, H. Lorenz, E.M. Weig, Size-independent Young's modulus of inverted conical GaAs nanowire resonators, Appl. Phys. Lett. 103 (26) (2013) 261901.
[41] M. Hjort, S. Lehmann, J. Knutsson, A.A. Zakharov, Y.A. Du, S. Sakong, R. Timm, G. Nylund, E. Lundgren, P. Kratzer, K.A. Dick, A. Mikkelsen, Electronic and Structural Differences between Wurtzite and Zinc Blende InAs Nanowire Surfaces: Experiment and Theory, ACS Nano 8 (2014) 12346–12355, https://doi.org/10.1021/nn504795v.
[42] J.H. Park, U. Chatterjee, S. Kang, D.Y. Um, C.R. Lee, The synthesis of hybrid nanostructure comprising star-shaped GaN nanowires and Si nanoworms, RSC Adv. 7 (2017) 24113–24121, https://doi.org/10.1039/c7ra03119j.